A Grid-compatible Virtual Oscillator Controller: Analysis and Design

Minghui Lu*, Soham Dutta*, Victor Purba†, Sairaj Dhople†, and Brian Johnson*
*Department of Electrical and Computer Engineering, University of Washington, Seattle, WA 98195
†Department of Electrical and Computer Engineering, University of Minnesota, Minneapolis, MN 55455
Emails: {mhlu, sdutta, brianbj}@uw.edu, and {purba002, sdhople}@umn.edu

***Abstract*—In this paper, we present a virtual oscillator control (VOC) strategy for power inverters to operate in either grid-connected or islanded settings. The proposed controller is based on the dynamics of the nonlinear Andronov-Hopf oscillator and it provides voltage regulation, frequency support in islanded mode. It also features the potential to respond to real- and reactive-power setpoints for dispatchability in grid-connected mode. In contrast to early VOC incarnations which exhibit undesirable harmonics, the proposed controller offers a sinusoidal ac limit cycle as well as improved dynamic performance. Moreover, the proposed controller intrinsically generates orthogonal signals which facilitate implementation in three-phase systems. We study the controller dynamical model and outline a systematic design procedure such that the inverter satisfies standard ac performance specifications. Numerical simulations validate the analytical developments.**

I. Introduction

Techniques to synchronize inverters in ac electric power systems have largely been based on droop-control methods that draw inspiration from the quasi-steady-state operation of synchronous generators [1]–[3]. Along similar lines, so-called virtual synchronous machine methods are focused on direct emulation of machine dynamics [4]–[6]. Departing from machine-inspired approaches, virtual oscillator control (VOC) is a control strategy where inverters are programmed to emulate the dynamics of weakly nonlinear limit-cycle oscillators such as dead-zone and Van der Pol oscillators [7]–[9]. These oscillators can generate periodic, self-sustained, and stable oscillations, and when leveraged as controllers for islanded inverters, they offer communication-free synchronization and power sharing [10], as well as voltage and frequency regulation [11]. Analysis also shows that VOC subsumes the functionality of conventional droop control in steady state while providing enhanced dynamic speed [12], [13] due to its time-domain implementation. The small-signal stability of a mixed machine-VOC inverter system has also been investigated in [14]. [15] applies the VOC in commercial current-controlled inverters with dual voltage and current loops.

M. Lu, S. Dutta and B. Johnson were supported by the US Department of Energy Solar Energy Technology office under grants DE-EE0000-1583 and DE-EE0008346. Support was also provided by the Washington Research Foundation and the Clean Energy Institute at the University of Washington. V. Purba and S. V. Dhople were supported in part by the National Science Foundation through grant 1509277.

Those previous controllers exhibited insurmountable trade-offs between harmonics (mainly 3$^{\text{rd}}$ order) and transient performance (i.e., a Van der Pol oscillator that is tuned to offer lower harmonic content can only do so at the expense of a sluggish response [11], [16]), which to some extent limits their adoption in the grid-connected application. Furthermore, existing VOC controllers are not well suited for three-phase system due to the existence of only one input for feedback [9], [17]. This implies that such controllers might be difficult to apply in unbalanced three-phase settings. Lastly, the dead-zone and Van der Pol oscillators themselves do not offer seamless control of real and reactive power, and hence, require additional loops if the ac-side power must be modulated to track references [9], [18], [19]. Along these lines, it is worth pointing out the dispatchable VOC methods, which are also called dVOC, that were recently reported in [20]–[22]. Interestingly, this type of controller is synthesized in a top-down system-level design procedure and ends up taking a similar form to the controller studied here. One key difference is that our design objectives are based on local inverter-level objectives which yield a simple design procedure.

To address the issues of previously proposed VOC strategies that are highlighted above, we introduce a grid-compatible oscillator for inverter control that emulates the dynamics of so-called Andronov-Hopf systems [23]. These dynamics are symmetric and planar, and they intrinsically embed orthogonal signals which are applicable to three-phase implementations. Remarkably, this oscillator type presents a perfectly circular limit cycle in steady-state with superior voltage and current quality. Furthermore, we can pre-specify the real-power, reactive-power, voltage and frequency set-points that makes it highly versatile for operation in both grid-connected and islanded settings. In this paper, we explicate the operating principles of the proposed controller and a systematic design procedure which ensures a wide range of user-defined performance criteria can be met at the inverter level.

The remainder of this paper is organized as follows: In Section II, we establish notation and the nonlinear oscillator dynamics. An implementation for three-phase inverters is outlined in Section III, and Section IV provides a control design procedure. Section V gives numerical simulations to illustrate dynamic performance. Finally, conclusions and pertinent directions for future work are in Section VI.

978-1-7281-0395-2/19/$31.00 ©2019 IEEE

II. Dynamical Model of Oscillator

In this section, we briefly outline mathematical notation and describe the dynamical oscillator model that underlies the proposed controller.

A. Notation

We consider balanced three-phase operation, where voltages and currents, $\{u_{\rm a}, u_{\rm b}, u_{\rm c}\}$ can be modeled equivalently in the $\alpha\beta$ domain as signals $\{u_\alpha, u_\beta\}$ if zero-sequence components are disregarded. Clarke's transformation [24] is used to obtain the $\alpha\beta$ components. By way of notation, $u_{\alpha\beta} := [u_\alpha, u_\beta]^\top \in \mathbb{R}^2$, where $(\cdot)^\top$ denotes the matrix transpose. Given $\theta \in [0, 2\pi]$, we define the rotation matrix

$$R(\theta) := \begin{bmatrix} \cos\theta & -\sin\theta \\ \sin\theta & \cos\theta \end{bmatrix}.$$

The Euclidean norm of vector, $x \in \mathbb{R}^N$ is denoted by $\|x\|$.

B. Nonlinear Oscillator

We introduce the nonlinear oscillator that underlies the proposed controller by first discussing the dynamical model of a harmonic oscillator. The general planar differential-equation model for the harmonic oscillator is given by

$$\begin{bmatrix} \dot{x}_1 \\ \dot{x}_2 \end{bmatrix} = \begin{bmatrix} 0 & -\omega_{\rm nom} \\ \omega_{\rm nom} & 0 \end{bmatrix} \begin{bmatrix} x_1 \\ x_2 \end{bmatrix}, \tag{1}$$

where x_1 and x_2 are the states, and $\omega_{\rm nom}$ denotes the resonant frequency at which the oscillator exhibits unforced sinusoidal oscillations. As a means to regulate the amplitude of oscillations (which are entirely initial-conditions dependent for the harmonic oscillator), we consider the following nonlinear extension to the model introduced above:

$$\begin{bmatrix} \dot{x}_1 \\ \dot{x}_2 \end{bmatrix} = \begin{bmatrix} \xi(2X_{\rm nom}^2 - \|x\|^2) & -\omega_{\rm nom} \\ \omega_{\rm nom} & \xi(2X_{\rm nom}^2 - \|x\|^2) \end{bmatrix} \begin{bmatrix} x_1 \\ x_2 \end{bmatrix}. \tag{2}$$

The above dynamical model yields oscillations with RMS amplitude $X_{\rm nom}$, and ξ is a constant that dictates the convergence speed to steady state (in subsequent developments, we refer to it as the speed constant). Figure 1 sketches trajectories yielded by the above model: the state trajectories always spiral asymptotically towards a stable circular limit cycle with a fixed radius $\sqrt{2}X_{\rm nom}$ and constant rotation frequency $\omega_{\rm nom}$ regardless of initial conditions. We now describe how the proposed controller derives from this nonlinear oscillator.

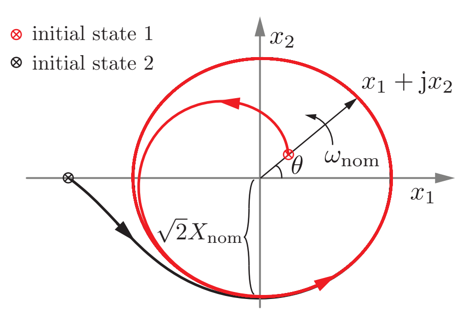

Figure 1: When unforced, the proposed oscillator has a circular limit cycle with radius $\sqrt{2}X_{\rm nom}$ and constant rotational frequency $\omega_{\rm nom}$. Any initial condition, aside from the origin, converges to this circular trajectory.

III. Inverter Controller Development and Dynamical Properties

In this section, we introduce the proposed controller for three-phase inverters. The controller leverages the nonlinear model introduced in (2), and permits voltage and frequency regulation while affording responses to active- and reactive-power setpoint changes.

A. Inverter Controller and Implementation

An illustration of the proposed controller and the manner in which it interfaces with the three-phase inverter is shown in Fig. 2. All elements included in the box marked "Microcontroller" are digitally realized. The physical inverter includes the dc source, a three-phase hex-bridge, and an output LCL filter consisting of inverter-side inductors $L_{\rm f}$, filter capacitors $C_{\rm f}$ and grid-side inductors $L_{\rm g}$. The controller is composed of two parts: i) A resonant LC tank, with its natural resonant frequency denoted by $\omega_{\rm nom} := 1/\sqrt{LC}$. The circuit states are the capacitor voltage and scaled inductor current:

$$x = [x_1, x_2]^\top = [v_{\rm C}, \varepsilon i_{\rm L}]^\top, \tag{3}$$

where $\varepsilon := \sqrt{L/C}$. ii) Nonlinear state-dependent voltage and current sources $v_{\rm m}$ and $i_{\rm m}$ given by

$$\begin{aligned} v_{\rm m} &:= \frac{\xi}{\omega_{\rm nom}} \left(2X_{\rm nom}^2 - \|x\|^2\right) x_2, \\ i_{\rm m} &:= \frac{\xi}{\varepsilon\omega_{\rm nom}} \left(2X_{\rm nom}^2 - \|x\|^2\right) x_1. \end{aligned} \tag{4}$$

The above expressions are derived from the nonlinear oscillator model introduced in (2). Basically, $v_{\rm m}$ and $i_{\rm m}$ collectively absorb energy from or provide energy to the circuit such that $\|x\| \to \sqrt{2}X_{\rm nom}$ asymptotically, and a circular trajectory with resonant frequency $\omega_{\rm nom}$ is maintained.

The oscillator is interfaced to the physical converter system through voltage and current scalings $\kappa_{\rm v}$ and $\kappa_{\rm i}$, respectively. We scale the orthogonal oscillator states, $v_{\rm C}$ and $\varepsilon i_{\rm L}$, by $\kappa_{\rm v}$ to generate the voltage commands, $v_{\alpha\beta}$, in the $\alpha\beta$ frame:

$$v_{\alpha\beta} := \kappa_{\rm v}[v_{\rm C}, \varepsilon i_{\rm L}]^\top. \tag{5}$$

The inverter terminal voltage $v_{\rm abc}$ is hence established through power stage and PWM. Furthermore, the inverter output currents, denoted by $i_{\rm abc}$, are measured and transformed to $i_{\alpha\beta}$, and then scaled by $\kappa_{\rm i}$ to act as the input signals, u_1 and u_2, which are derived from the difference between measured line currents $i_{\alpha\beta}$ and current setpoints $i_{\alpha\beta}^\star$, as follows:

$$u := \begin{bmatrix} u_1 \\ u_2 \end{bmatrix} = \kappa_{\rm i} R(\varphi)(i_{\alpha\beta} - i_{\alpha\beta}^\star). \tag{6}$$

Above, φ is a user-defined rotation angle. In subsequent developments pertaining to voltage and frequency regulation, we will illustrate how φ is a key parameter that determines the relationship between voltage amplitude and frequency versus

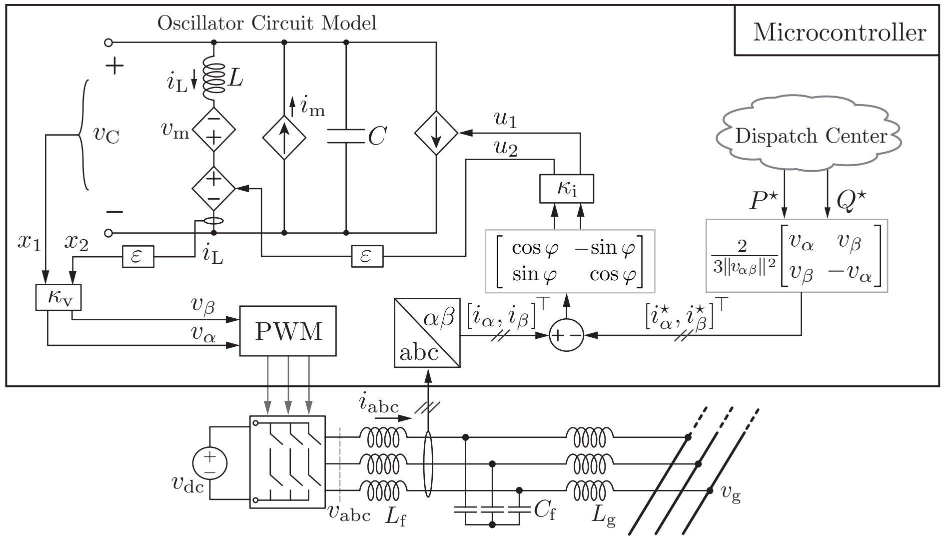

Figure 2: A three-phase inverter with the proposed nonlinear oscillator-based controller.

real and reactive power. Finally, the proposed controller can respond to real- and reactive-power setpoints, $P^\star$ and $Q^\star$ (issued potentially from an external dispatch center). These are converted into current commands in the $\alpha\beta$ frame as follows:

$$\begin{bmatrix} i_\alpha^\star \\ i_\beta^\star \end{bmatrix} = \frac{2}{3\|v_{\alpha\beta}\|^2} \begin{bmatrix} v_\alpha & v_\beta \\ v_\beta & -v_\alpha \end{bmatrix} \begin{bmatrix} P^\star \\ Q^\star \end{bmatrix}. \tag{7}$$

B. Voltage and Frequency Dynamics

We now proceed to discuss the inverter voltage- and frequency-regulation characteristics. To do so, we first begin with the oscillator circuit-states dynamics, which in this case are those corresponding to the capacitor voltage v_C and inductor current i_L. From the circuit representation in Fig. 2, we see that these dynamics are given by:

$$\begin{aligned} C\frac{\mathrm{d}v_\mathrm{C}}{\mathrm{d}t} &= -i_\mathrm{L} + \frac{\xi}{\varepsilon\omega_\mathrm{nom}}(2X_\mathrm{nom}^2 - \|x\|^2)v_\mathrm{C} - u_1, \\ L\frac{\mathrm{d}i_\mathrm{L}}{\mathrm{d}t} &= v_\mathrm{C} + \frac{\xi}{\omega_\mathrm{nom}}(2X_\mathrm{nom}^2 - \|x\|^2)\varepsilon i_\mathrm{L} - \varepsilon u_2. \end{aligned} \tag{8}$$

Then, the following dynamics are obtained for $v_{\alpha\beta} = \kappa_\mathrm{v}[v_\mathrm{C}, \varepsilon i_\mathrm{L}]^\top$ by appropriately substituting (6) into (8)

$$\begin{aligned} \begin{bmatrix} \dot{v}_\alpha \\ \dot{v}_\beta \end{bmatrix} &= \begin{bmatrix} \frac{\xi}{\kappa_\mathrm{v}^2}\left(2V_\mathrm{nom}^2 - \|v_{\alpha\beta}\|^2\right) & -\omega_\mathrm{nom} \\ \omega_\mathrm{nom} & \frac{\xi}{\kappa_\mathrm{v}^2}\left(2V_\mathrm{nom}^2 - \|v_{\alpha\beta}\|^2\right) \end{bmatrix} \begin{bmatrix} v_\alpha \\ v_\beta \end{bmatrix} \\ &\quad - \frac{\kappa_\mathrm{v}\kappa_\mathrm{i}}{C} \begin{bmatrix} \cos\varphi & -\sin\varphi \\ \sin\varphi & \cos\varphi \end{bmatrix} \begin{bmatrix} i_\alpha - i_\alpha^\star \\ i_\beta - i_\beta^\star \end{bmatrix}, \end{aligned} \tag{9}$$

where $V_\mathrm{nom} := \kappa_\mathrm{v} X_\mathrm{nom}$ is nominal inverter voltage RMS amplitude. For grid-connected mode, V_nom can be set to either grid nominal voltage $V_\mathrm{g,nom}$ or the measured grid voltage amplitude. The expressions for the voltage RMS amplitude V and phase angle θ are given by

$$V = \frac{1}{\sqrt{2}}\left(v_\alpha^2 + v_\beta^2\right)^{\frac{1}{2}}, \quad \theta = \arctan\left(\frac{v_\beta}{v_\alpha}\right). \tag{10}$$

From these elementary definitions and (9), the following dynamical model for amplitude V and phase angle θ is obtained

$$\begin{aligned} \dot{V} &= \frac{v_\alpha\dot{v}_\alpha + v_\beta\dot{v}_\beta}{2V} = \frac{\xi}{\kappa_\mathrm{v}^2}V\left(2V_\mathrm{nom}^2 - 2V^2\right) \\ &\quad - \frac{\kappa_\mathrm{v}\kappa_\mathrm{i}}{3CV}\left(\sin\varphi(Q - Q^\star) + \cos\varphi(P - P^\star)\right), \end{aligned} \tag{11}$$

$$\begin{aligned} \dot{\theta} &= \frac{v_\alpha\dot{v}_\beta - v_\beta\dot{v}_\alpha}{2V^2} = \omega_\mathrm{nom} \\ &\quad - \frac{\kappa_\mathrm{v}\kappa_\mathrm{i}}{3CV^2}\left(\sin\varphi(P - P^\star) - \cos\varphi(Q - Q^\star)\right). \end{aligned} \tag{12}$$

It can be observed that the dynamics of both voltage amplitude V and phase angle θ vary with the difference between the actual real- (reactive-) power and reference real- (reactive-) power, and also with different rotation angle φ.

C. Steady-state Voltage and Frequency Regulation

With appropriate decoupling assumptions, various dynamical model for amplitude V and frequency ω can be recovered from (11) and (12): with $\varphi = 0$, the proposed controller trades off V versus P and ω versus Q, with $\varphi = \pi/2$, V is traded off for Q and ω is traded off for P. For subsequent developments, we select $\varphi = \pi/2$, which is applicable to inductive networks. Then, (11) and (12) turn to:

$$\begin{aligned} \dot{V} &= \frac{\xi}{\kappa_\mathrm{v}^2}V\left(2V_\mathrm{nom}^2 - 2V^2\right) - \frac{\kappa_\mathrm{v}\kappa_\mathrm{i}}{3CV}(Q - Q^\star), \\ \dot{\theta} &= \omega_\mathrm{nom} - \frac{\kappa_\mathrm{v}\kappa_\mathrm{i}}{3CV^2}(P - P^\star). \end{aligned} \tag{13}$$

Setting the derivatives $\dot{V} = 0$ and $\dot{\theta} = \omega$ yields the steady-state voltage amplitude, V, and frequency, ω, relations as follows:

$$\begin{aligned} V &= \frac{V_\mathrm{nom}}{\sqrt{2}}\left(1 + \sqrt{1 - \frac{2\kappa_\mathrm{i}\kappa_\mathrm{v}^3}{3C\xi V_\mathrm{nom}^4}(Q - Q^\star)}\right)^{\frac{1}{2}}, \\ \omega &= \omega_\mathrm{nom} - \frac{\kappa_\mathrm{v}\kappa_\mathrm{i}}{3CV^2}(P - P^\star). \end{aligned} \tag{14}$$

While the trade-off is linear for $P-\omega$, it is nonlinear for $Q-V$. Nonetheless, we will show numerically that the $Q-V$ curve is close to linear. We also know from (14) that in grid-connected mode the inverter locks on the grid frequency, $\omega \rightarrow \omega_{\text{nom}}$, and real power P will track $P^{\star}$. In islanded mode, deviations from nominal conditions can be compensated with the power setpoints.

D. Transient Dynamics

Given the dynamical models in place for the voltage magnitude and frequency, a variety of transient performance specifications could be readily investigated. We focus on: i) the voltage rise time, t_{rise}, and ii) the time to transition between two real-power setpoints. In particular, we outline a design strategy for the controller parameters that yield specified values of the above transient performance specifications. The maximum allowable voltage rise time and power-transition time constant are denoted by $t_{\text{rise}}^{\max}$ and $\tau^{\max}$, respectively.

1) Voltage Rise Time: This time period describes how fast an unloaded inverter establishes its terminal voltage. By setting $Q = Q^{\star}$ and multiplying both sides of (13) by V, we have

$$V\dot{V} = \frac{\xi}{\kappa_{\text{v}}^2} V^2 \left(2V_{\text{nom}}^2 - 2V^2\right). \tag{15}$$

Note that since the above is an ordinary differential equation, we can get the voltage rise time t_{rise} by integrating both sides from $0.1V_{\text{nom}}$ to $0.9V_{\text{nom}}$ (we pick these limits without loss of generality). Defining $M = V^2$ and $M_{\text{nom}} = V_{\text{nom}}^2$, we have

$$\dot{M} = \frac{4\xi}{\kappa_{\text{v}}^2} M \left(M_{\text{nom}} - M\right), \tag{16}$$

from which we can express:

$$\text{d}t = \frac{\kappa_{\text{v}}^2}{4\xi} \frac{1}{M\left(M_{\text{nom}} - M\right)} \text{d}M. \tag{17}$$

Integrating both sides,

$$\begin{aligned} t_{\text{rise}} &= \frac{\kappa_{\text{v}}^2}{4\xi} \int_{0.01M_{\text{nom}}}^{0.81M_{\text{nom}}} \frac{1}{M\left(M_{\text{nom}} - M\right)} \text{d}M \\ &= \frac{3\kappa_{\text{v}}^2}{2\xi M_{\text{nom}}} = \frac{3\kappa_{\text{v}}^2}{2\xi V_{\text{nom}}^2}. \end{aligned} \tag{18}$$

Substituting $V_{\text{nom}} = \kappa_{\text{v}} X_{\text{nom}}$ yields

$$t_{\text{rise}} = \frac{3}{2X_{\text{nom}}^2 \xi}. \tag{19}$$

This indicates that the rise time t_{rise} is inversely proportional to oscillation amplitude X_{nom}^2 and speed constant ξ. It means that we can tune the parameter ξ to set the voltage rise time.

2) Power-transition Time Constant τ: Next, we demonstrate that real power dynamics are approximately first-order, and the time constant τ of the response can be adjusted by tuning pertinent system and oscillator parameters. In an inductive network, three-phase real power P is

$$P = 3\frac{VV_{\text{g}}}{X} \sin(\theta - \theta_{\text{g}}) \approx 3\frac{VV_{\text{g}}}{X}(\theta - \theta_{\text{g}}), \tag{20}$$

where V_{g} is the grid RMS voltage, θ_{g} is the grid phase angle, and $X = \omega_{\text{nom}}(L_{\text{f}} + L_{\text{g}})$ is the filter and line impedance (see Fig. 2). The filter capacitance C_{f} is neglected because it only addresses switching frequency components. Due to the fact $\Delta\theta = \theta - \theta_{\text{g}} \approx 0$, we assume $\sin\Delta\theta \approx \Delta\theta$. Using (13), $\Delta\dot{\theta}$ can be expressed as given below when $\dot{\theta}_{\text{g}} \approx \omega_{\text{nom}}$:

$$\Delta\dot{\theta} = -\frac{\kappa_{\text{v}}\kappa_{\text{i}}}{3CV^2}(P - P^{\star}). \tag{21}$$

From (20) and (21), we obtain

$$\dot{P} = -\frac{\kappa_{\text{v}}\kappa_{\text{i}}}{CX}(P - P^{\star}). \tag{22}$$

In the Laplace domain, we get:

$$P = \frac{1}{\tau s + 1} P^{\star}, \quad \tau = \frac{CX}{\kappa_{\text{v}}\kappa_{\text{i}}}. \tag{23}$$

Evidently, P tracks $P^{\star}$ via first-order dynamics with time constant τ. We can tune C to obtain desirable power dynamics.

IV. Oscillator Design Procedure

In this section, we outline a design procedure to select the oscillator parameters such that the inverter satisfies a set of user-defined performance specifications.

A. Design Objectives

The performance specifications that we expect the inverter to conform to are summarized in Table I. These include: 1) Nominal RMS line-neutral output voltage V_{nom} and minimum permissible voltage, $V_{\text{min,pu}}$; 2) Rated apparent power S_{rated}, real power P_{rated}, and reactive power Q_{rated}; 3) Nominal frequency ω_{nom} and frequency regulation $|\Delta\omega|_{\max}$; 4) Maximum rise time $t_{\text{rise}}^{\max}$ and power-tracking time constant $\tau^{\max}$. The oscillator parameters to be designed are listed in Table II. They include: nominal oscillation amplitude X_{nom},

TABLE I
THREE-PHASE INVERTER PERFORMANCE SPECIFICATIONS.

Symbol	Description	Value	Units
S_{rated}	Rated apparent power	1200	W
P_{rated}	Rated real power	850	W
Q_{rated}	Rated reactive power	850	VAR
V_{nom}	Nominal output voltage	80	V RMS
$V_{\text{min, pu}}$	Per-unit minimum voltage	0.95	–
ω_{nom}	Nominal frequency	$2\pi 60$	rad/s
$\lvert\Delta\omega\rvert_{\max}$	Maximum frequency offset	$2\pi 0.5$	rad/s
$t_{\text{rise}}^{\max}$	Maximum voltage rise time	120	ms
$\tau^{\max}$	Power-transition time constant	40	ms

TABLE II
NONLINEAR OSCILLATOR PARAMETERS.

Symbol	Description	Value	Units
X_{nom}	Nominal oscillation amplitude	1	V
κ_{v}	Voltage-scaling factor	80	V/V
κ_{i}	Current-scaling factor	0.20	A/A
ξ	Speed constant	15	$1/\text{sV}^2$
C	Virtual capacitance	0.2679	F
L	Virtual inductance	26.268	μH

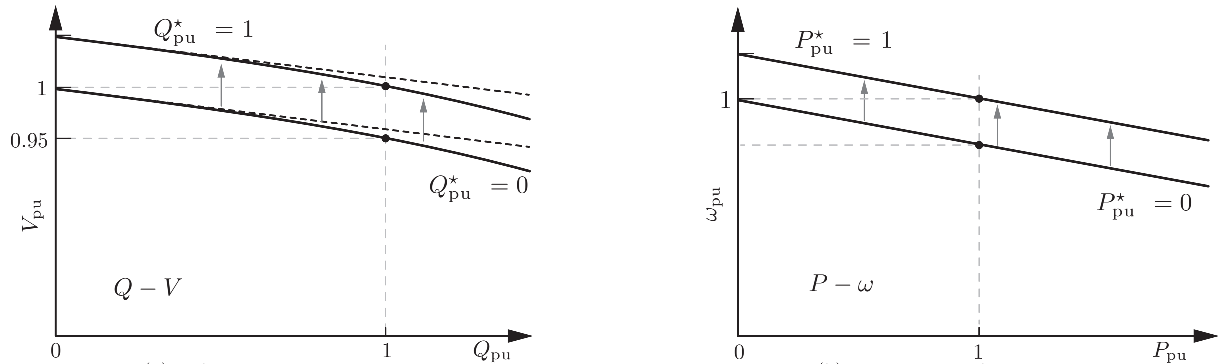

(a) Voltage-reactive power curve (b) Frequency-real power curve

Figure 3: Steady-state per-unit inverter voltage- and frequency-regulation.

scaling factors $\kappa_{\rm v}$ and $\kappa_{\rm i}$, speed constant ξ, and oscillator inductance and capacitance L and C, respectively.

To facilitate system design, we seek an oscillator which yields unity normalized RMS amplitudes of its states $[x_1, x_2]^\top$ and inputs $[u_1, u_2]^\top$ (i.e., $X_{\rm nom} = 1\,{\rm V}$ and $\|u\|/\sqrt{2} = 1\,{\rm A}$) when the inverter is fully loaded $P = Q = 1$ ($\|i_{\alpha\beta}\|/\sqrt{2} = S_{\rm rated}/3V_{\rm nom}$), with setpoints $P^\star = Q^\star = 0$ ($i^\star_{\alpha\beta} = 0$). Under such conditions, it follows that the voltage and current scaling factors must be chosen as

$$\kappa_{\rm v} := V_{\rm nom}, \quad \kappa_{\rm i} := 3\frac{V_{\rm nom}}{S_{\rm rated}}. \tag{24}$$

B. The Per-unit Model

Next, we transfer the amplitude and frequency dynamics in (13) to a per-unit model, in which all signals are expressed as fractions of their defined base values. This simplifies the design process since per-unit values do not vary with inverter ratings. Consider the following per-unit quantities:

$$\begin{aligned} V_{\rm pu} &= \frac{V}{V_{\rm nom}}, \quad \omega_{\rm pu} = \frac{\omega}{\omega_{\rm nom}}, \\ P_{\rm pu} &= \frac{P}{P_{\rm rated}}, \quad Q_{\rm pu} = \frac{Q}{Q_{\rm rated}}. \end{aligned} \tag{25}$$

Substitution of (24) and (25) into (13) yields the following per-unit dynamical-system model

$$\dot{V}_{\rm pu} = 2\xi V_{\rm pu}(1 - V_{\rm pu}^2) - \frac{1}{\sqrt{2}CV_{\rm pu}}(Q_{\rm pu} - Q^\star_{\rm pu}), \tag{26}$$

$$\omega_{\rm pu} = 1 - \frac{1}{\sqrt{2}C\omega_{\rm nom}V_{\rm pu}^2}(P_{\rm pu} - P^\star_{\rm pu}). \tag{27}$$

Note that $S_{\rm rated} = \sqrt{2}P_{\rm rated} = \sqrt{2}Q_{\rm rated}$. Solving $\dot{V}_{\rm pu} = 0$ gives the following steady-state per-unit $V_{\rm pu}$ expression (analogous to (14)) as

$$V_{\rm pu} = \sqrt{\frac{1 + \sqrt{1 - \frac{\sqrt{2}}{C\xi}(Q_{\rm pu} - Q^\star_{\rm pu})}}{2}}. \tag{28}$$

As shown above, the steady-state $Q-V$ relationship depends on ξ and the capacitance C whereas the $P-\omega$ relationship only depends on C. This is true because the amplitude $V_{\rm pu}$ is close to unity and has only a second-order influence on the phase dynamics. Figures 3(a) and (b) show the resulting $Q-V$ and $P-\omega$ curves for (27) and (28). In these figures, we observe that the power setpoints $P^\star_{\rm pu}$ and $Q^\star_{\rm pu}$ only make the curves move up and down, but have no impact on the droop slopes. Hence, in the subsequent design, we fix the $P^\star_{\rm pu} = Q^\star_{\rm pu} = 0$.

C. Design of ξ and Capacitance C

The maximum steady-state voltage and frequency deviations occur when the expressions in (28) are evaluated at $P_{\rm rated}$ ($P_{\rm pu} = 1$) and $Q_{\rm rated}$ ($Q_{\rm pu} = 1$). Given a user-defined minimum terminal voltage $V_{\rm min,pu}$ (which occurs at $Q_{\rm pu} = 1$) and maximum allowable frequency deviation $|\Delta\omega|_{\max}$ (which occurs at $P_{\rm pu} = 1$), we have

$$V_{\rm min,\,pu} = \sqrt{\frac{1 + \sqrt{1 - \frac{\sqrt{2}}{C\xi}}}{2}}, \tag{29}$$

$$\Delta\omega = \frac{1}{\sqrt{2}CV_{\rm min,\,pu}^2} \le |\Delta\omega|_{\max}. \tag{30}$$

Then, we get the following constraint for the product $C\xi$, and the following lower bound for C:

$$C\xi = \frac{\sqrt{2}}{4V_{\rm min,\,pu}^2}\frac{1}{1 - V_{\rm min,\,pu}^2}, \tag{31}$$

$$C \ge \frac{1}{\sqrt{2}V_{\rm min,\,pu}^2}\frac{1}{|\Delta\omega|_{\max}} =: C_{\min}. \tag{32}$$

In order to meet the transient response specifications, we also obtain the following constraints for ξ and C:

$$t_{\rm rise} = \frac{3}{2\xi} \le t_{\rm rise}^{\max}, \quad \xi \ge \frac{3}{2t_{\rm rise}^{\max}} =: \xi_{\min}, \tag{33}$$

$$\tau = \frac{XC}{\kappa_{\rm v}\kappa_{\rm i}} \le \tau^{\max}, \quad C \le \tau^{\max}\frac{3V_{\rm nom}^2}{XS_{\rm rated}} =: C_{\max}. \tag{34}$$

D. A Complete Design Procedure

From the developments above, $X_{\rm nom}$, $\kappa_{\rm v}$, and $\kappa_{\rm i}$ can be computed unambiguously as (24). The feasible set of ξ and C values which satisfy all performance specifications are given by the constraints in (31)–(34) (see also Fig. 4). Once

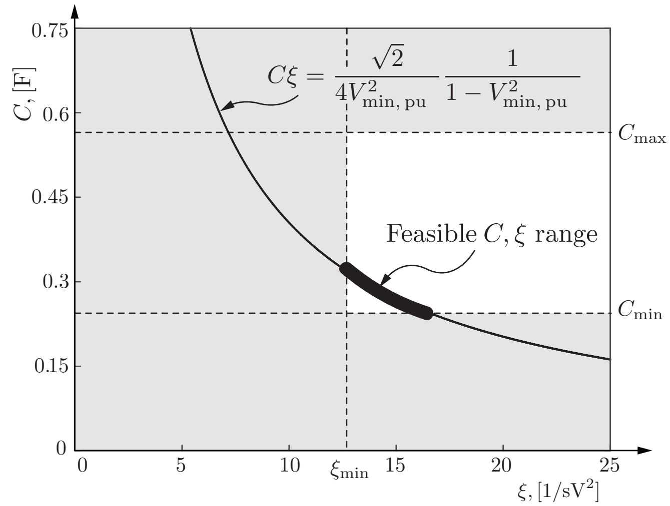

Figure 4: Values of ξ and C that satisfy performance specifications.

a value of capacitance C is chosen, the virtual inductance, L, is a dependent design variable since $\omega_{\text{nom}} = 1/\sqrt{LC}$, and the nominal system frequency is specified. According to the constraints in (32) and (33), oscillator parameters ξ and capacitance C can be selected as shown in Fig. 4. In this design, both filter inductance are chosen as $1.5\,\text{mH}$, $X = 1.131\,\Omega$. The overall choice of oscillator parameters is listed in Table II.

V. Simulation Results

We now illustrate the performance of the proposed inverter controller through detailed simulation results for grid-connected and islanded modes of operation.

A. Power Tracking

When connected to a stiff grid, the oscillator-controlled inverter is able to track the power setpoints $P^\star$, $Q^\star$. During grid-connected mode in Fig. 5, we show the case where $Q^\star$ is fixed at zero and the real power setpoints evolve as $P^\star$: $0\,\text{W} \rightarrow 500\,\text{W} \rightarrow 1000\,\text{W} \rightarrow 500\,\text{W}$. Observe that the actual real power P closely tracks the power setpoints. Once

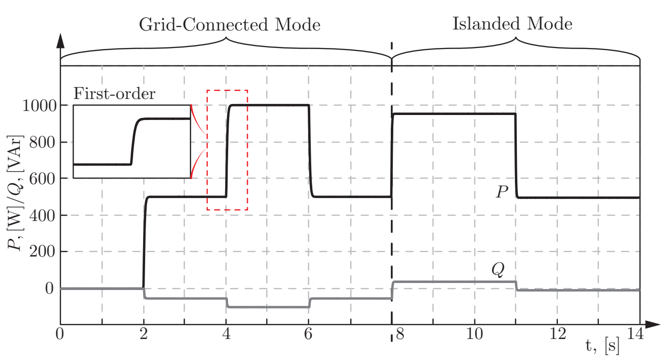

Figure 5: Real- and reactive-power transients in the grid-connected (0 to 8 s) and islanded modes (8 - 14 s), step changes of $P^\star$ happen at 2, 4, 6 s, load step change at 11 s.

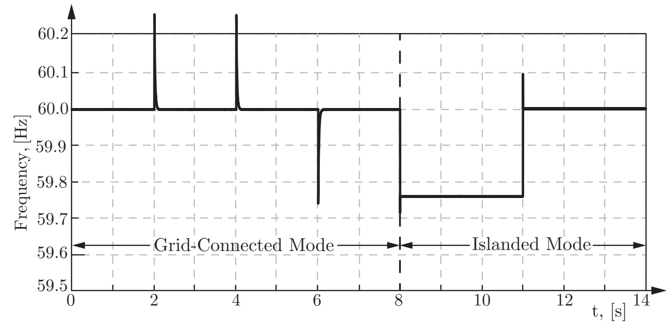

Figure 6: Inverter voltage frequency transients between grid-connected and islanded modes of operation.

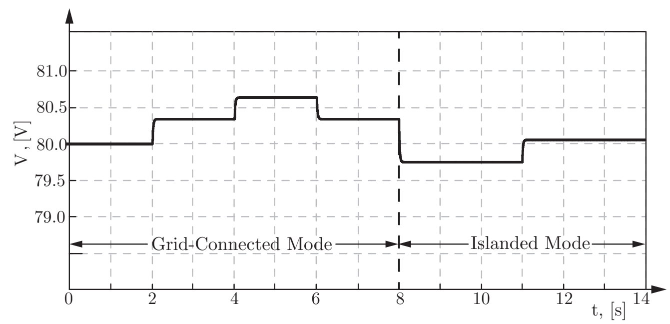

Figure 7: Corresponding inverter voltage amplitude RMS value transients.

the system is islanded at $t = 8\,\text{s}$, the setpoints are fixed at $P^\star = 500\,\text{W}$ and the inverter supplies a resistive load ($R_{\text{L}} = 20\,\Omega$, $P_{\text{Load}} = 960\,\text{W}$). A load step is initiated at $t = 11\,\text{s}$ where P_{Load} decreases from $960\,\text{W}$ to $480\,\text{W}$.

B. Voltage and Frequency Regulation

Figures 6 and 7 show the inverter frequency ω and amplitude RMS value V, respectively. During grid-connected mode, we assume the grid has a stiff voltage amplitude and frequency at nominal values. In such a setting, the oscillator locks onto the grid frequency and $\omega \rightarrow \omega_{\text{nom}}$ in steady-state. Under islanded conditions, the frequency decreases to $59.77\,\text{Hz}$ in accordance with (26) and (27). At the load step down event at $t = 11\,\text{s}$, we can see that the inverter frequency tracks back to grid frequency, $60\,\text{Hz}$, because $P_{\text{Load}} \approx P^\star$ at this point.

C. Transient Performance

To substantiate the transient dynamic performance of real power P and voltage V, Fig. 8 shows the voltage and current waveforms. It can be observed that the current dynamics are first-order and has the same time constant as the power dynamics in Fig. 5. Figure 9 shows the voltage rise time from $0.1V_{\text{nom}}$ to $0.9V_{\text{nom}}$. We observed that it took around $105\,\text{ms}$ for inverter to establish the terminal voltage, which meets the design transient specification $t_{\text{rise}}^{\max}$.

VI. Conclusions & Future Work

In this paper, we analyzed and designed a dispatchable oscillator inverter controller. Compared to existing VOC implementations, it eliminates low-frequency harmonics, can

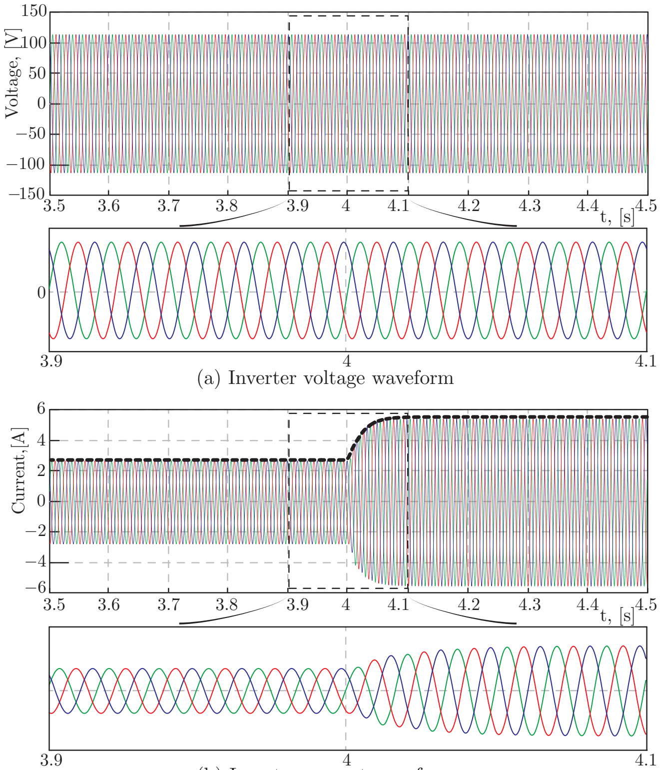

(a) Inverter voltage waveform

(b) Inverter current waveform

Figure 8: Inverter output three-phase voltage and current waveforms during [3.5 s, 4.5 s], real power reference $P^{\star}$ step changes at $t = 4$ s, (a) voltage waveform, (b) current waveform.

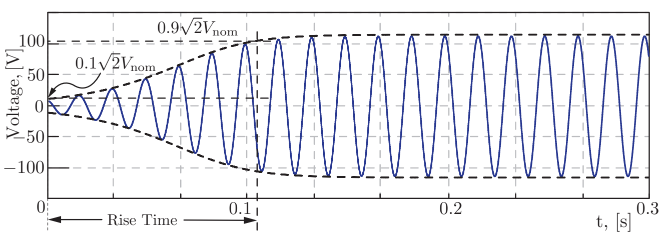

Figure 9: Voltage rise time t_{rise}, voltage increases from $0.1V_{\mathrm{nom}}$ to $0.9V_{\mathrm{nom}}$.

be designed faster, and operate in both islanded and grid-connected settings. Future work includes experimental validation and investigation of the proposed controller in complex networks.

References

[1] M. C. Chandorkar, D. M. Divan, and R. Adapa, "Control of parallel connected inverters in standalone AC supply systems," *IEEE Transactions on Industry Applications*, vol. 29, pp. 136–143, Jan. 1993.

[2] N. Pogaku, M. Prodanovic, and T. C. Green, "Modeling, Analysis and Testing of Autonomous Operation of an Inverter-Based Microgrid," *IEEE Transactions on Power Electronics*, vol. 22, pp. 613–625, Mar. 2007.

[3] Q.-C. Zhong, "Robust droop controller for accurate proportional load sharing among inverters operated in parallel," *IEEE Transactions on Industrial Electronics*, vol. 60, pp. 1281–1290, Apr. 2013.

[4] Q.-C. Zhong and G. Weiss, "Synchronverters: Inverters that mimic synchronous generators," *IEEE Transactions on Industrial Electronics*, vol. 58, pp. 1259–1267, Apr. 2011.

[5] T. Shintai, Y. Miura, and T. Ise, "Oscillation damping of a distributed generator using a virtual synchronous generator," *IEEE Transactions on Power Delivery*, vol. 29, pp. 668–676, Apr. 2014.

[6] J. Liu, Y. Miura, H. Bevrani, and T. Ise, "Enhanced virtual synchronous generator control for parallel inverters in microgrids," *IEEE Transactions on Smart Grid*, vol. 8, pp. 2268–2277, Sep. 2017.

[7] L. A. Torres, J. P. Hespanha, and J. Moehlis, "Synchronization of Identical Oscillators Coupled Through a Symmetric Network With Dynamics: A Constructive Approach With Applications to Parallel Operation of Inverters," *IEEE Transactions on Automatic Control*, vol. 60, pp. 3226–3241, Dec. 2015.

[8] S. V. Dhople, B. B. Johnson, and A. O. Hamadeh, "Virtual oscillator control for voltage source inverters," in *2013 51st Annual Allerton Conference on Communication, Control, and Computing (Allerton)*, pp. 1359–1363, Oct. 2013.

[9] D. Raisz, T. T. Thai, and A. Monti, "Power control of virtual oscillator controlled inverters in grid-connected mode," *IEEE Transactions on Power Electronics*, vol. 34, pp. 5916–5926, Jun. 2019.

[10] B. B. Johnson, S. V. Dhople, A. O. Hamadeh, and P. T. Krein, "Synchronization of Nonlinear Oscillators in an LTI Electrical Power Network," *IEEE Transactions on Circuits and Systems I: Regular Papers*, vol. 61, pp. 834–844, Mar. 2014.

[11] B. Johnson, M. Sinha, N. Ainsworth, F. Dörfler, and S. Dhople, "Synthesizing Virtual Oscillators to Control Islanded Inverters," *IEEE Transactions on Power Electronics*, vol. 31, pp. 6002–6015, Aug. 2016.

[12] M. Sinha, F. Dörfler, B. B. Johnson, and S. V. Dhople, "Uncovering Droop Control Laws Embedded Within the Nonlinear Dynamics of Van der Pol Oscillators," *IEEE Transactions on Control of Network Systems*, vol. 4, pp. 347–358, Jun. 2017.

[13] Z. Shi, J. Li, H. Nurdin, and J. E. Fletcher, "Comparison of virtual oscillator and droop controlled islanded three-phase microgrids," *IEEE Transactions on Energy Conversion*, pp. 1–1, 2019.

[14] M. M. Siraj Khan, Y. Lin, B. Johnson, M. Sinha, and S. Dhople, "Stability assessment of a system comprising a single machine and a virtual oscillator controlled inverter with scalable ratings," in *IECON 2018 - 44th Annual Conference of the IEEE Industrial Electronics Society*, pp. 4057–4062, Oct. 2018.

[15] M. Lu, G. Seo, M. Sinha, F. Rodriguez, S. Dhople, and B. Johnson, "Adaptation of commercial current-controlled inverters for operation with virtual oscillator control," in *2019 IEEE Applied Power Electronics Conference and Exposition (APEC)*, pp. 3427–3432, Mar. 2019.

[16] M. Ali, H. I. Nurdin, and J. E. Fletcher, "Simultaneous Regulation of Active and Reactive Output Power of Parallel-Connected Virtual Oscillator Controlled Inverters," in *IECON 2018 - 44th Annual Conference of the IEEE Industrial Electronics Society*, pp. 4051–4056, Oct. 2018.

[17] B. Johnson, S. V. Dhople, J. L. Cale, A. O. Hamadeh, and P. T. Krein, "Oscillator-Based Inverter Control for Islanded Three-Phase Microgrids," *IEEE Journal of Photovoltaics*, vol. 4, pp. 387–395, Jan. 2014.

[18] M. A. Awal, H. Yu, H. Tu, S. Lukic, and I. Husain, "Hierarchical control for virtual oscillator based grid-connected and islanded microgrids," *IEEE Transactions on Power Electronics*, pp. 1–1, 2019.

[19] M. Ali, H. I. Nurdin, and J. E. Fletcher, "Output power regulation of a virtual oscillator controlled inverter," in *2018 IEEE 18th International Power Electronics and Motion Control Conference (PEMC)*, pp. 1085–1090, Aug. 2018.

[20] G. Seo, M. Colombino, I. Subotic, B. Johnson, D. Groß, and F. Dörfler, "Dispatchable virtual oscillator control for decentralized inverter-dominated power systems: Analysis and experiments," in *2019 IEEE Applied Power Electronics Conference and Exposition (APEC)*, pp. 561–566, Mar. 2019.

[21] D. Groß, M. Colombino, J. Brouillon, and F. Dörfler, "The effect of transmission-line dynamics on grid-forming dispatchable virtual oscillator control," *IEEE Transactions on Control of Network Systems*, pp. 1–1, 2019.

[22] M. Colombino, D. Gross, J. Brouillon, and F. Dörfler, "Global phase and magnitude synchronization of coupled oscillators with application to the control of grid-forming power inverters," *IEEE Transactions on Automatic Control*, pp. 1–1, 2019.

[23] Y. A. Kuznetsov, "Andronov-Hopf bifurcation," *Scholarpedia*, vol. 1, no. 10, p. 1858, 2006.

[24] A. Yazdani and R. Iravani, *Voltage-Sourced Converters in Power Systems*. Hoboken, NJ: John Wiley & Sons, Inc., 2010.